JGR Space Physics

RESEARCH ARTICLE
10.1029/2024JA033044

Characteristics of Sporadic E Layer Occurrence in a Global Chemistry-Climate Model: A Comparison With COSMIC-Derived Data

Tasha Aylett[1], Wuhu Feng[1,2], Daniel R. Marsh[1,3], David R. Themens[4], and John M. C. Plane[1]

[1]School of Chemistry, University of Leeds, Leeds, UK, [2]National Centre for Atmospheric Science, University of Leeds, Leeds, UK, [3]School of Physics and Astronomy, University of Leeds, Leeds, UK, [4]School of Engineering, University of Birmingham, Birmingham, UK

Key Points:

- Sporadic E layers are formed self-consistently in the Extended Whole Atmosphere Community Climate Model with additional metal ion transport
- Sporadic E layers are identified in model output using a novel algorithm based on specified selection criteria
- There is good qualitative agreement between the climatology of identified Es layers and Es derived from COSMIC satellite observations

Supporting Information:

Supporting Information may be found in the online version of this article.

Correspondence to:

T. Aylett,
n.m.aylett@leeds.ac.uk

Citation:

Aylett, T., Feng, W., Marsh, D. R., Themens, D. R., & Plane, J. M. C. (2025). Characteristics of sporadic E layer occurrence in a global chemistry-climate model: A comparison with COSMIC-derived data. *Journal of Geophysical Research: Space Physics*, *130*, e2024JA033044. https://doi.org/10.1029/2024JA033044

Received 12 JUL 2024
Accepted 13 DEC 2024

Abstract This study presents an analysis of sporadic-E (Es) structures within WACCM-X (the Whole Atmosphere Community Climate Model with thermosphere and ionosphere eXtension), including electrodynamical transport of metallic ions. A set of selection criteria have been developed to identify Es layers in WACCM-X output based on the total metal ion density in each model grid box. These criteria are used to create a climatology of Es, which is compared to Es occurrence rates derived from FORMOSAT/COSMIC-1 (Constellation Observing System for Meteorology, Ionosphere, and Climate) radio-occultation measurements. The novel identification algorithm analyses 2-week time slices between altitudes of 90–150 km, with Es layer events identified where the three selection criteria are met. Distinct seasonal distributions in Es occurrence were observed that are consistent with previous studies, with peaks during summer and reduced frequencies during winter, alignment of Es with geomagnetic contours, and layers descending in altitude as a function of local time. While discrepancies exist between WACCM-X and COSMIC data (WACCM-X occurrence rates are a factor of ~2 lower than COSMIC-derived occurrence rates at mid-latitudes), highlighting the ongoing challenges in modeling Es layers, this study enhances the modeling capabilities of sporadic Es and deepens our understanding of their formation; it establishes a basis for their enhanced integration into global climate models and facilitates further investigation of Es behavior under different atmospheric conditions, paving the way to improved prediction of the occurrence of Es.

1. Introduction

Sporadic E (Es) layers are transient ionospheric phenomena that occur in the E region (~90–150 km) and are characterized by thin, localized layers of enhanced electron density. Their formation mechanisms are complex and are linked to interactions involving atmospheric waves and tides (Axford, 1963; Djuth et al., 2010; Haldoupis et al., 2006; Oikonomou et al., 2014), wind shear and/or electric field (Arras et al., 2009; Nygrén et al., 1984; Shinagawa et al., 2017; J Whitehead, 1961; Yu, Xue, et al., 2021), lower atmosphere forcing and geomagnetic activity (Pedatella, 2016; Thayer & Semeter, 2004), plasma instabilities (Farley, 1985; Hysell et al., 2002; Mathews, 1998), and chemical reactions of metallic ions (Cox & Plane, 1998; Plane, 2003).

Es layers have been studied extensively since the invention of the ionosonde in the 1930s, and their formation and dynamics are reasonably well understood (Mathews, 1998; J D Whitehead, 1989). However, a complete description is still elusive - reconstructing ionospheric Es layers on a global basis presents a unique challenge due to the multiple mechanisms that contribute to their formation and the different spatial-temporal variations at different latitudes (Kirkwood & Nilsson, 2000; Raghavarao et al., 2002). Nonetheless, with notable impacts on satellite communications, radio wave propagation and global navigation systems (Cameron et al., 2022; Chartier et al., 2022; Pavelyev et al., 2007; Wang et al., 2021; Yue et al., 2016), their accurate representation in global climate models is of interest to a wide range of disciplines (Fernandez-Prades et al., 2011).

To understand Es layers and their impact on the atmosphere, comprehensive observational data and sophisticated modeling techniques are required. Ground-based observations using Incoherent Scatter Radars (ISRs) or Ionosondes can provide high temporal resolution and precise analyses of characteristics such as height, electron density, critical frequency (foEs) and occurrence frequency (Gooch et al., 2020; Haldoupis et al., 2006; Mathews, 1998; Pignalberi et al., 2014; Wang et al., 2022; Yu, Scott, et al., 2021). However, they provide limited

coverage, and the reliability of measurements can be affected by adverse weather and atmospheric variability. Space-based techniques (Arras et al., 2008; Chu et al., 2014; Hocke & Tsuda, 2001; Hu et al., 2022; D L Wu et al., 2005; Yu et al., 2019) provide broader coverage: satellite observations using GPS-techniques or ionospheric sounders can probe the regional or global occurrence and distribution (though offer coarser vertical resolution than ground-based observations). However, coverage may be limited in certain areas or time-periods, and the sensitivity and frequency-range of instruments can affect their ability to capture relevant characteristics (Sobhkhiz-Miandehi et al., 2023). Furthermore, satellite-based techniques ultimately provide an indirect measure of Es occurrence. Sobhkhiz-Miandehi et al. (2023) demonstrate that up to 20% of conjunctions with ionosonde data disagreed; however, the proportion of such disagreements due to the RO technique itself is unclear, as ionosondes themselves suffer low sensitivity to Sporadic-E at low densities, which are most prevalent during winter and low solar activity periods. This 20% disagreement can thereby be taken as a very conservative upper bound on the potential uncertainty in the approach.

One notable observational dataset derives from the COSMIC satellite constellation (Anthes et al., 2008). COSMIC is comprised of six microsatellites performing radio occultation (RO) measurements that collect data on both the neutral atmosphere and ionosphere. There are many different techniques to obtain Es statistics from RO measurements, with significant differences in the occurrence frequencies that are derived (Arras & Wickert, 2018; Chu et al., 2014; Emmons et al., 2023; Gooch et al., 2020; Niu et al., 2019; D L Wu et al., 2005; Yu et al., 2020). This variation is primarily because they map to different Es intensity thresholds (Carmona et al., 2022). One such method uses amplitude and phase fluctuations that occur when a radio wave traverses plasma density irregularities (Kintner et al., 2007). Es layers cause these scintillations because of the large vertical gradient in electron density (Pavelyev et al., 2007; Zeng & Sokolovskiy, 2010). The S4 index defines the scintillation strength and is defined as the ratio of the standard deviation of signal intensity fluctuations normalized to the mean signal intensity. The maximum value of S4 (denoted $S4_{max}$) is widely used to quantify ionospheric irregularities (Arras et al., 2009; Arras & Wickert, 2018; Ye et al., 2021; Yu et al., 2020). Typically, if $S4_{max}$ exceeds a defined threshold within a specified altitude range, this scintillation is defined as an Es layer. More recently, efforts have focused on the use of machine learning techniques in conjunction with RO measurements to improve Es classification (Ellis et al., 2024).

In addition to observational approaches, a range of modeling techniques have been employed in the study of Es layers. These are broadly categorized into physics-based models, data-driven models, and integrated physics/chemistry models. Physics-based models focus on simulating the physical processes governing Es layer formation, such as ion transport, winds, and momentum. For example, Resende et al. (2017) used an ionospheric E region model (MIRE) to study blanketing sporadic E-layers, obtaining good agreement with ionograms recorded in the Brazilian region. Huba et al. (2019) and Krall et al. (2020) were able to reproduce Arecibo ISR observations using the SAMI3 (Sami3 is Also a Model of the Ionosphere) model and the empirical HWM14 (Horizontal Wind Model) models. Andoh et al. (2023) were able to reproduce the day-to-day variability of Es layers observed at Arecibo using the GAIA (Ground-to-topside model of Atmosphere and Ionosphere for Aeronomy) model. Furthermore, Shinagawa et al. (2021) explored the relationship between vertical ionospheric convergence and Es intensity in GAIA and compared their results to ionosonde observations, finding limited performance that they attributed to limited knowledge of the input metallic ion distribution and influx, as well as challenges in lower boundary forcing.

Recently, data-driven models that rely on empirical methods and observational data have also been used to simulate Es layers. Yu et al. (2022) developed an empirical model of Es layers using the multivariable nonlinear least-squares-fitting method with COSMIC RO measurements. This model captured the diurnal and seasonal variations of Es layers, but not the significant variability of Es layers during summer. Recently, Tian et al. (2023) reconstructed Es layer morphology using SELF-ANN (Artificial Neural Networks), a prediction engine trained using observational data from multiple sources. A simplified version of this tool is publicly available and can make predictions between the years 2002–2025.

Integrated physics/chemistry models have also been employed for the study of Es layers. For example, Chu et al. (2014) used Fe^+ concentrations ($[Fe^+]$) from the coupled chemistry-climate model WACCM (the Whole Atmosphere Community Climate Model) combined with HWM07 (the Horizontal Wind Model) and the Mass Spectrometer and Incoherent Scatter (MSIS-00) atmospheric model to calculate the divergence of the vertical $[Fe^+]$ flux for comparison with COSMIC-derived Es occurrence. An examination was made of the relation

between COSMIC-derived Es layers and neutral wind shear, concluding that the wind shear convergence mechanism is the primary mechanism driving the formation of COSMIC-derived Es layers.

To achieve a comprehensive understanding of the underlying physical processes responsible for the formation and extent of Es layers globally, further experimental and theoretical studies are warranted. Whole-atmosphere climate models are valuable tools for examining the occurrence, formation and variability of Es layers in the context of broader-scale atmospheric processes and climate dynamics, enabling a range of different atmospheric conditions and scenarios to be probed. However, the spatial and temporal resolution required to capture this mesoscale phenomenon creates computational challenges. Furthermore, limitations in the availability of observations to inform and validate simulations pose additional constraints (Abdu et al., 1996; Hodos et al., 2022; Oyinloye, 1969; Rao, 1964; Solomon et al., 2019; Tsunoda, 2008).

Metal ions are tightly coupled with electrons through ionization and neutralisation processes and play a central role in the formation of Es layers (Layzer, 1972; Plane et al., 2015; Yu, Xue, et al., 2021). The ambient molecular ions O_2^+ and NO^+ recombine with electrons quickly through dissociative recombination, meaning they have short lifetimes (a few to several minutes) and therefore cannot sustain Es (Haldoupis, 2019). In contrast, metallic ions are neutralised by forming a molecular cluster ion via termolecular recombination with N_2 or O_2, or through bimolecular reaction with O_3 in the case of Fe^+ and Mg^+, followed by dissociative electron recombination. However, these molecular metal-containing ions are converted back to atomic metal ions by reaction with atomic O, which increases rapidly above 90 km; hence, their lifetimes are from a few hours to several days at altitudes of from 95 to 120 km (Plane, 2003; Plane et al., 2015).

Although modelling of parameters relevant to Es layers (winds, temperatures, chemical constituents) has been carried out using whole atmosphere models (Chu et al., 2014; Yu, Xue, et al., 2021), modelling of Es layers has not been carried out self-consistently within a global climate model with metal ion transport. Recently, J Wu et al. (2021) implemented the full transport of three metal ions (Fe^+, Mg^+ and Na^+) in WACCM-X (a self-consistent global model including the full neutral and ion-molecule chemistry of the metals and their injection from meteoric ablation (Carrillo-Sánchez et al., 2020; Feng et al., 2013; Langowski et al., 2015; H-L Liu, Bardeen, et al., 2018; Marsh, Janches, et al., 2013)). The work of J Wu et al. (2021) significantly improved the modelled global distribution and seasonal dependence of the metal ions in WACCM-X. Because it captures the complex interactions between numerous atmospheric components, this extended WACCM-X provides a useful framework for the study of Es layers on a global scale.

In the present study, we first describe an algorithm to detect Es layers in WACCM-X with full transport of metal ions, and then use this to determine the climatology of Es occurrence. The derived climatology is compared to global high-resolution ionospheric observations from the COSMIC satellite constellation. This comparison enables us to evaluate the performance of the model and identify potential areas for further development. The insights gained from this research advance modelling capabilities, and could support space weather forecasting and communication systems, as well as contributing to the broader understanding of Es layers and their significance in atmospheric science.

2. Methodology

2.1. Model Description

WACCM-X is the atmospheric component of the NCAR-developed Community Earth System Model (CESM, version 2.1.3) (Hurrell et al., 2013) extended to the ionosphere and thermosphere, with a model top at 4×10^{-10} hPa (500–700 km depending on solar activity). It uses a hybrid sigma-pressure vertical coordinate with 126 levels, having a vertical resolution of a quarter of a scale height in the mesosphere and thermosphere. The horizontal resolution is 1.9° latitude and 2.5° longitude. Chemical and dynamical aspects are drawn from CAM4 and WACCM4, described by (Marsh, Mills, et al., 2013) and Neale et al. (2013). Validated metal chemistry modules for iron (Feng et al., 2013), magnesium (Langowski et al., 2015), and sodium (Marsh, Janches, et al., 2013) are added, with updated rate coefficients from Plane et al. (2015), Bones et al. (2016), and Viehl et al. (2016). Meteoric input functions (MIFs) are estimated using CABMOD-3 (Chemical Ablation Model version 3) coupled to the ZoDY (Zodiacal Dust) astronomical model (Carrillo-Sánchez et al., 2020).

A detailed description of WACCM-X with enhanced metallic ion transport is given in J Wu et al. (2021). This version improves the model performance of metal ions from the lower thermosphere to 300 km. In brief, standard

WACCM-X has been enhanced to include the full life cycle of Mg, Na, and Fe in addition to their interactive chemistry, dynamics, deposition, and global ion transport in the E and F regions. Metal ion transport is calculated in line with the treatment of the most active chemical species O_3 and CO_2, as described by H-L Liu et al. (2018a). Model results are from 1-year free-running simulations (perpetual year 2000), with an output frequency of 1 hr. Solar and geomagnetic forcing are parameterized by the F10.7 cm solar flux (F10.7) and geomagnetic activity index (Kp), respectively (Tapping, 2013; H-L Liu, Bardeen, et al., 2018; Matzka et al., 2021); the Es layer identification algorithm development was performed under moderate solar conditions (F10.7 = 130) and quiet geomagnetic conditions (represented by Kp = 1).

2.2. Identification Algorithm Development

The algorithm iteratively analyses 2-week time slices (1–14th and 15th-28th of each month) between 1.3×10^{-3} hPa and 1.5×10^{-5} hPa (~90–150 km in altitude). Working in 30-min local time (LT) intervals, selection criteria identify whether Es layers are present in each 4D model grid box (a function of pressure, latitude, local time and universal time). By summing the statistics over time and dividing by the total number of time points in each time slice, an occurrence frequency is calculated, which is averaged over each season to give the overall climatology (the seasons are defined as March-May, June-August, September-November, and December-February). Since Es layers depend primarily on metal plasma density rather than that of ambient ions, M^+ density fluctuations are used as a proxy for Es layers, where $[M^+] = [Fe^+] + 2[Mg^+] + [Na^+]$. The Mg^+ ion concentration is doubled because the model does not currently treat Si^+, and so $[Mg^+]$ is used to represent Si^+ since both elements have essentially the same injection rate from meteoric ablation.

There do not appear to have been any previous studies specifying selection criteria for metal ions to determine the statistical occurrence of Es layers. However, two previous studies have examined the occurrence of sporadic neutral Fe and Na layers using LIDAR and satellite data, respectively (Dieterich et al., 2006; Fan et al., 2007). With regard to selection criteria, both studies defined lower limits to the metal density: Dieterich et al. (2006) specified that the maximum of the sporadic Fe layer density must be greater than twice the uncertainty of the sporadic Fe density and a minimum density of 500 cm^{-3}; whereas Fan et al. (2007) defined a limit of half the peak density of the standard Na layer (determined from zonally averaged Na profiles in each 10° latitude bin, averaged for each month). Additionally, the density of the peak of the sporadic Na layer had to be more than three times larger than the standard Na layer density at the same altitude. These criteria were used here as a basis for the algorithm, with sensitivity studies conducted to determine the most suitable criteria for capturing fluctuations in the total metal ion density (further details of the sensitivity studies can be found in the supplementary information). Since Es layers represent a marked deviation from the background ion density, the criteria establish tangible thresholds to represent the physical properties of Es layers, linking to both the ion density at each specific location and the typical background ion density.

Three empirically defined selection criteria were used - see Figure 1 for a visual example of these criteria at both a mid- and low-latitude location. The first criterion stipulates that the difference between the total metal ion density ($[M^+]$) and the average total metal ion density for that grid box over the time slice ($[M^+]_{av}$) must be greater than 0.25× the standard deviation (σ_{M+}). The second criterion specifies that $[M^+]$ must be greater than two times the zonal average total metal ion density in the corresponding 5° latitude slice ($[M^+]_{za}$). Third, the maximum of $[M^+]_{za}$ is calculated over the height dimension to obtain the peak of the layer ($max_{lev}([M^+]_{za})$), and $[M^+]$ must be larger than this value. That is.

1. $[M^+] - [M^+]_{av} > 0.25\ \sigma_{M+}$
2. $[M^+] > 2\ [M^+]_{za}$
3. $[M^+] > max_{lev}([M^+]_{za})$

While sensitivity studies reveal reliable detection of Es layers, we recognize the potential for further refinement of the identification criteria. For instance, in the left panel of Figure 1, an Es layer is identified at 90 km, which may indicate a need for fine-tuning. Additionally, since different criteria lead to different statistical results, we will focus our assessment on a qualitative representation of observed features.

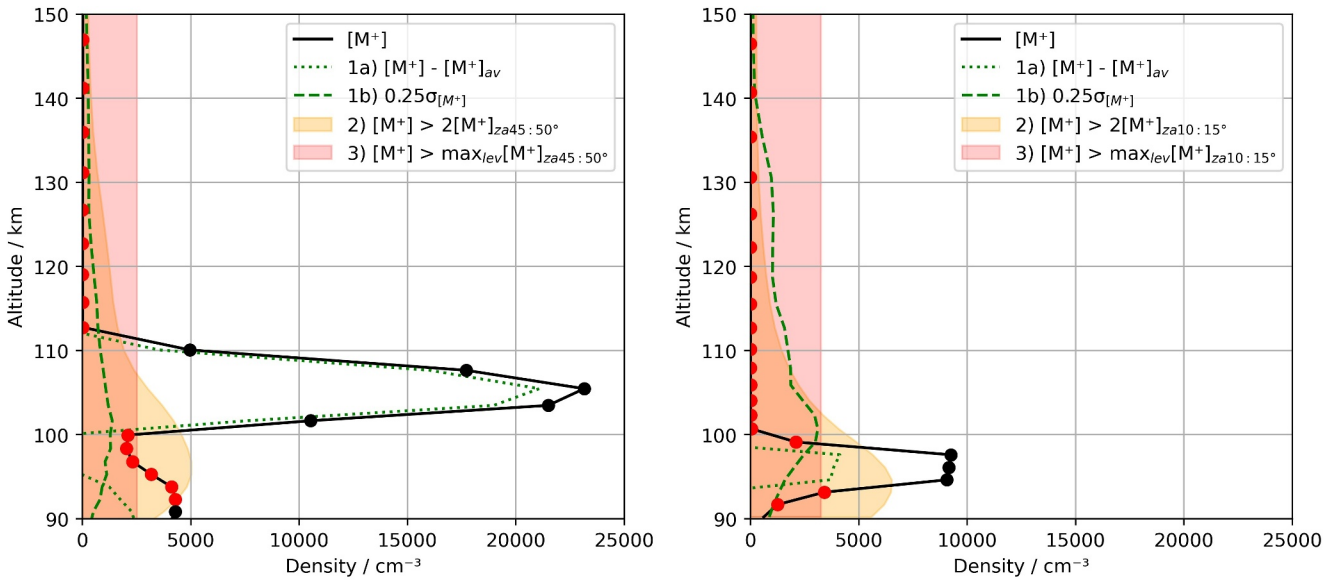

Figure 1. Examples illustrating the Es layer selection criteria for two Es events. (left) 06-01-07:00 UT at 48°N, 45°E (right) 06-01-07:00 UT at 12.5°N, 52.5°W. Shaded sections show areas excluded by criterion 2 (orange) and criterion 3 (pink). The components of criterion 1 (defined as 1a > 1b) are represented in green, where 1a) is $[M^+] - [M^+]_{av}$ and 1b) is $0.25\sigma_{[M+]}$. Black circles identify data points where an Es event is identified (all three criteria are met) and red circles show data points excluded by the criteria.

2.3. COSMIC Radio Occultation Data Processing

Satellite data from the COSMIC reprocessed dataset were analyzed from 2009 to 2019, following the method of Arras and coworkers (Arras et al., 2022; Arras & Wickert, 2018). Occultations were considered between altitudes of 70–150 km. However, if the upper altitude limit of an individual occultation was less than 125 km it was removed from the dataset, since the range was insufficient to cover the full range of altitudes where we may expect Es and is thereby insufficient to be able to discern whether Es was actually present. Es layers were assigned under the conditions: $S4_{max} > 0.2$; the altitude range over which S4 > 0.2 is less than 10 km wide; and the standard deviation of S4 over the full range <0.11 (Arras et al., 2022; Arras & Wickert, 2018).

The distribution of COSMIC measurements varies with latitude due to orbital configurations, resulting in a higher abundance of measurements in mid-latitudes (15–60°). Furthermore, as the mission progressed the decommissioning of satellites resulted in a decrease of available measurements, thereby introducing a sampling bias in the occurrence frequencies calculated, particularly at high and low latitudes (see Figure S6 in Supporting Information S1). To minimize this latter effect, only Es occurrence data from 2007 to 2009 and 2013 were considered for comparison with WACCM-X occurrence frequencies, coinciding with periods of the highest data abundance and spanning both low and high solar activity periods.

3. Results and Discussion

Figure 2 shows the latitudinal variation of Es layer occurrence rates across March-May, June-August, September-November, and December-February (northern hemisphere (NH) spring, summer, autumn and winter). Employing the specified selection criteria to identify Es layers, WACCM-X yields Es occurrence rates that are about half that of COSMIC Es estimated from $S4_{max}$. In Figure 2, COSMIC occurrence rates are scaled down by 2 for comparison (an equivalent figure with unscaled COSMIC data is presented in Figure S7 in Supporting Information S1). For each season, uncertainties were calculated using Clopper-Pearson confidence intervals (95%) for each 2-week time sample, taking the minimum (maximum) of the lower (upper) bounds to capture the variability in occurrence frequencies. The closest agreement between COSMIC and WACCM-X occurrence frequencies occurs at mid-high latitudes, with the largest discrepancies occurring at mid-low latitudes. While observational uncertainties may account for some of the differences at mid-high latitudes, other factors likely contribute to the discrepancy in Es occurrence rates, as discussed below.

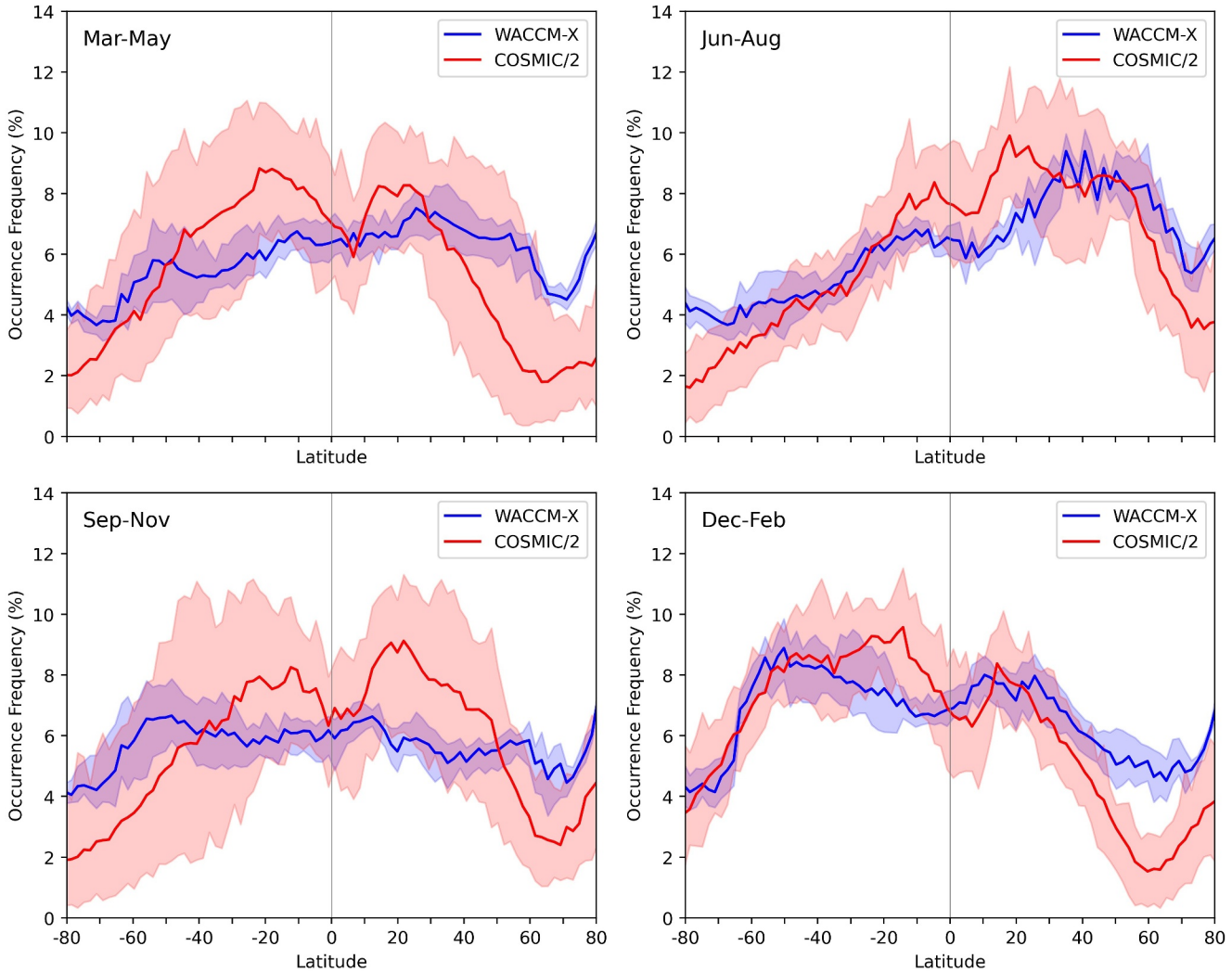

Figure 2. Latitude distributions of the seasonal Es layer occurrence rates (%), for different seasons, for WACCM-X (blue) and COSMIC (red). COSMIC-derived occurrence rates are scaled down by a factor of 2 to facilitate comparison.

While WACCM captures the main features of the diurnal and semidiurnal tide, the model is known to underestimate tidal amplitudes at mid-latitudes in the mesosphere-lower thermosphere (MLT), which could help elucidate these results, since mid-latitude Es are predominantly tidally-driven (Feng et al., 2015). Sub-grid scale gravity waves are not explicitly resolved in WACCM-X; this may also contribute to the lower occurrence rate of Es layers, since gravity wave forcing can generate density perturbations in Es layers. Qui et al. (2023) found that including gravity waves in their numerical simulations led to $[M^+]$ enhancements of up to 60% between 90 and 120 km, and variations of up to ∼+600%/−90% between 120 and 150 km. Similarly, Zhou et al. (2024) used a 1D model to simulate the effects of gravity waves on Es layers and concluded that while these effects are complex and varied, mesoscale gravity waves can play a critical role in sustaining Es layers, particularly above 100 km. The under-representation of these waves in the model could lead to a weaker enhancement of ion densities, contributing to the discrepancies observed between WACCM-X and COSMIC.

It is important to acknowledge that achieving a direct comparison between the WACCM-X and COSMIC is challenging for a number of reasons. For example, the identification of Es layers from COSMIC uses occultations at specific locations, before binning the derived statistics to the coarser model resolution for comparison. In contrast, the identification of Es layers in WACCM-X calculates Es layer statistics directly at the model resolution. As such, WACCM-X will potentially miss fine-scale features that could be captured in the COSMIC dataset, because local density variations at sub-grid scales cannot be resolved in the model. Lower amplitudes in

the metal ion density fluctuations due to this "smoothing out" effect will be less likely to meet the Es selection criteria and therefore lead to lower occurrence rates. This effect will be more prominent at equatorial latitudes and high altitudes where the grid spacing is largest, therefore WACCM-X will have decreased sensitivity to low-latitude and high-altitude Es.

Even if the resolution were identical, the inherent differences in data outputs, thresholds and sensitivities between the COSMIC and WACCM-X derivation methods might still result in differences in the identified Es layer occurrences. For example, the COSMIC dataset incorporates Es layers based on the combined effect of both metal ions and ambient ions, whereas in WACCM-X only metal ion density is used to identify Es. Though metal ions are the primary driver of Es layers, it is possible that focusing solely on metal ions density could result in missing Es layers where ambient ions have a more significant contribution to the density fluctuations.

Nonetheless, consistent with the observations, WACCM-X displays inter-seasonal variability in Es formation, characterized by a pronounced summer maximum and winter minimum. This seasonality can be understood in terms of the variability in metal ion density that is governed by the seasonal dependence of sporadic meteor deposition and the lower thermospheric meridional circulation (Haldoupis et al., 2007; Yu, Xue, et al., 2021). In WACCM-X, the seasonally varying MIF, which peaks in autumn in each hemisphere, was validated against radar meteor head echo observations (Janches et al., 2006) and is able to reproduce the observed metal layers in terms of peak concentration and seasonal variation (extratropical Fe^+, Mg^+ and Na^+ exhibit a summer maximum, whereas in the tropics metal ion densities are more constant) (Feng et al., 2013; Langowski et al., 2015; Marsh, Janches, et al., 2013). In June-August, a distinct peak in Es occurrence can be seen in the northern (summer) hemisphere with lower frequencies observed across the southern (winter) hemisphere. In contrast, during December-February there is lower Es occurrence in the northern hemisphere, and higher occurrence in the southern hemisphere. At the equinoxes, during the months of March-May and September-November, a more symmetrical latitudinal distribution is observed.

Figure 3 displays the latitude-longitude distributions of the COSMIC and WACCM-X derived Es occurrence rates binned within a grid of 5° × 5°. As for Figure 2, the COSMIC-derived occurrence frequencies have been adjusted by a factor of 2 to facilitate easier comparison. Overall, the climatological features observed by (Haldoupis et al., 2007) are evident in the WACCM simulations, that is, a summer peak and winter trough. In June–August (December–February) a maximum is observed in the Es occurrence in the northern (southern) hemisphere, with more consistent formation across longitudes at mid-to low-latitudes.

Es layer occurrence aligns closely with geomagnetic contours, highlighting the influence of the Earth's magnetic field on Es formation. The geomagnetic field impacts where and how effectively Es layers form by influencing the vertical convergence of ions, a key factor in Es layer formation (Haldoupis, 2012). The contribution of the vertical shear of the zonal wind to ion convergence scales with the cosine of the geomagnetic inclination (I) (Shinagawa et al., 2017), meaning this contribution is stronger at lower latitudes where the inclination is smaller; while the geomagnetic field facilitates ion convergence across all latitudes, the higher occurrence of Es layers at mid-latitudes is primarily driven by stronger wind shears from the semidiurnal tide (J Wu et al., 2021).

Differences in both electric field effects and gravity wave structures are likely to be important for Es formation at high and low latitudes (Chu et al., 2014; Kirkwood & Nilsson, 2000; J Liu, Liu, et al., 2018; MacDougall & Jayachandran, 2005; MacDougall et al., 2000)—these processes are treated with an empirical model and parametrization schemes in WACCM-X, which could lead to discrepancies when compared with observational data and highlight the need for further refinement of the model to accurately capture the complexities of Es layer formation (Garcia et al., 2017; H-L Liu, Bardeen, et al., 2018; Richter et al., 2010). For example, since precipitating electrons are represented using a parametrization scheme in the auroral oval (H-L Liu, Bardeen, et al., 2018), the Southern Atlantic Anomaly (SAA) is not represented in WACCM-X; as such, the decrease in Es occurrence seen around the SAA in COSMIC for the equinox seasons is not observed in WACCM-X. Likewise, the marked reduction in Es occurrence seen in COSMIC data at the magnetic equator is not replicated in WACCM-X, as the electrodynamic processes that influence Es suppression in the equatorial region are also not fully represented in the model.

The discrepancy between the COSMIC and WACCM-X derived occurrence rates at high latitudes could also be attributed to variations in solar activity: the COSMIC measurements used for the analysis are mostly during time-periods associated with low solar/geomagnetic activity, though the real-world conditions are time-varying.

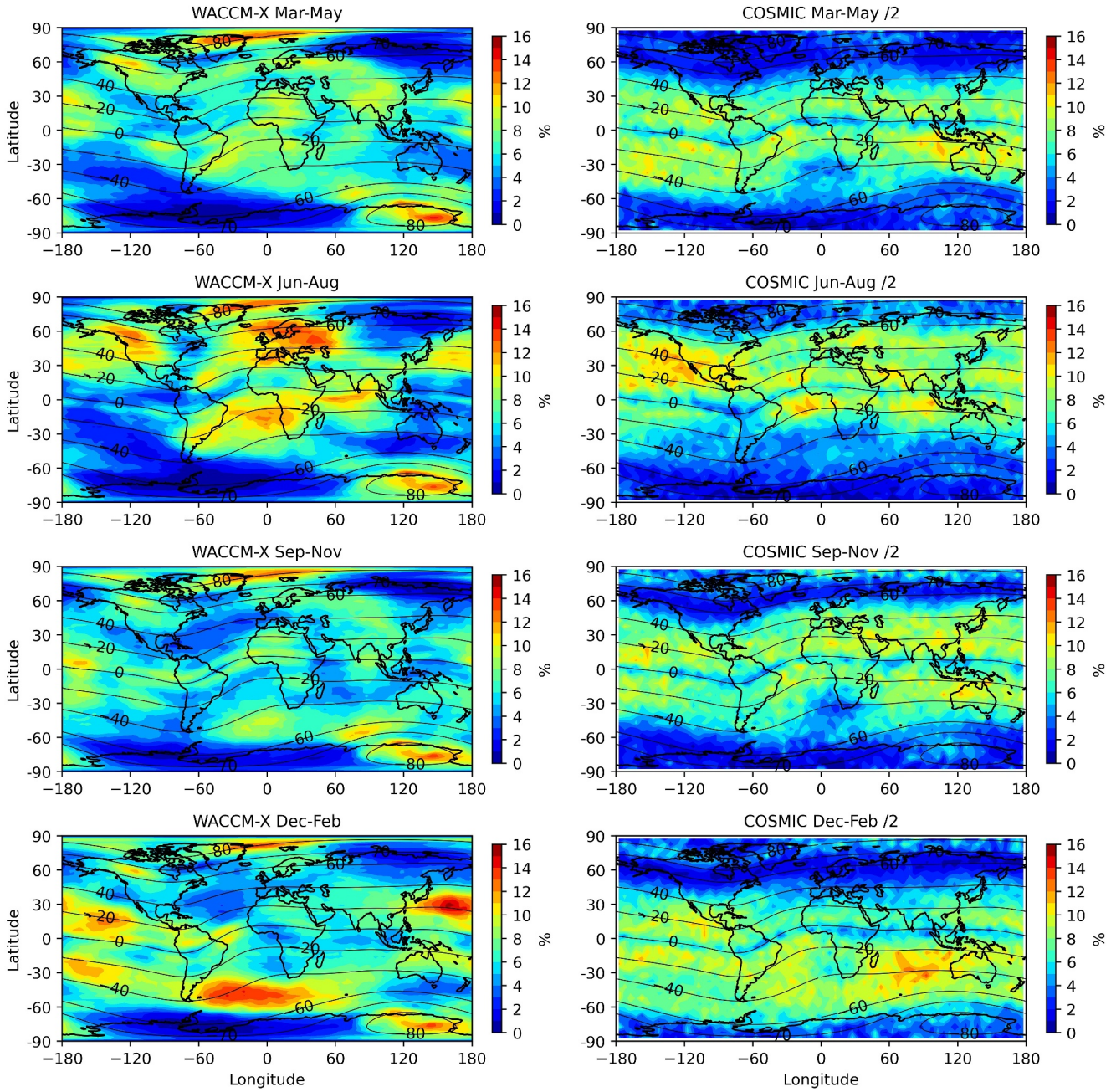

Figure 3. Latitude-longitude distributions of seasonal Es layer occurrence rates (%) for WACCM-X (left), and COSMIC (right) scaled down by a factor of 2.

WACCM-X simulations were conducted under constant moderate solar conditions (f10.7 = 130) and quiet geomagnetic conditions (kp = 1). The influence of solar activity on Es layer occurrence is unclear - both positive, negative, and no correlations have been reported in the literature (Fontes et al., 2024; Kotadia, 1969; Pavelyev et al., 2007; Pezzopane et al., 2015; Sivakandan et al., 2023; Zhang et al., 2015; Zuo & Wan, 2002). Changes in Es layer formation with solar activity may be attributed to changes in production of metal ions via photoionization (Pezzopane et al., 2015), changes in stratospheric heating and therefore tidal amplitudes (Vial, 1993), or changes in zonal winds leading to variations in gravity wave drag, residual circulation, and temperatures in the MLT (Cullens et al., 2016). The concentration of atomic oxygen and ozone also varies over the solar cycle, which play a role in the metal ion chemistry. Such effects may directly or indirectly influence Es layer formation.

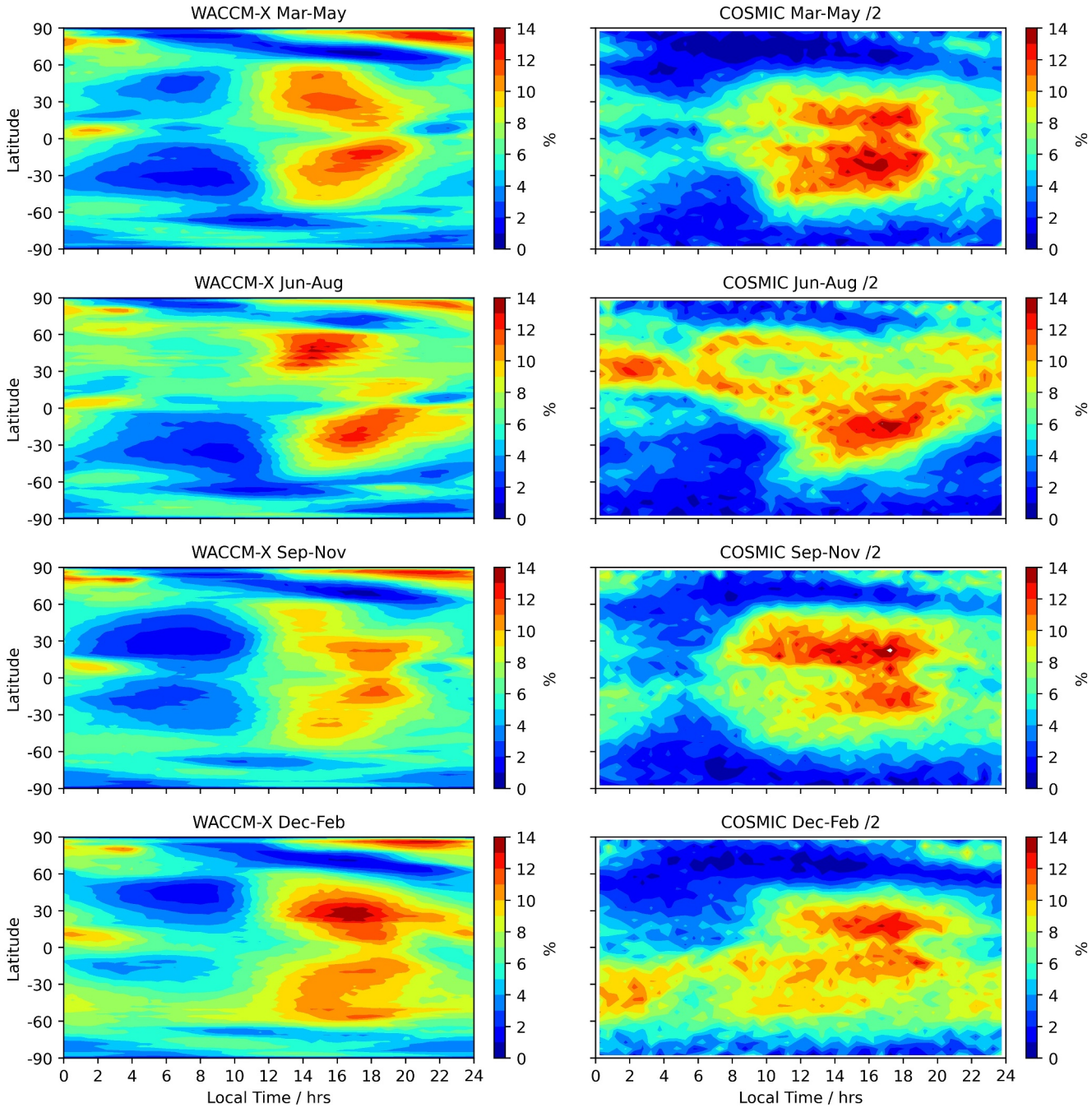

Figure 4. Latitude-local time distributions of the seasonal Es layer occurrence rates (%), for WACCM-X (left), and COSMIC (right) scaled down by a factor of 2.

Figure 4 illustrates the latitude-local time distributions of Es layer occurrence rates across the seasons. For the COSMIC-derived occurrences, Es layers are prevalent at low to mid-latitudes - typically between 09:00 and 22:00 LT, with a peak in occurrence around 16:00–18:00 LT and reduced frequency between 02:00–08:00 LT. In the summer hemispheres, Es formation demonstrates more consistent patterns throughout both local day and night periods. In the WACCM-X simulations, a similar temporal pattern emerges, with Es formation typically occurring between 10:00 and 00:00 LT, and peaking around 16:00 and 18:00 LT. During equinoxes, a decrease in Es occurrence is observed overnight in both hemispheres, while in summer (for both the NH and SH) Es formation persists during the local night.

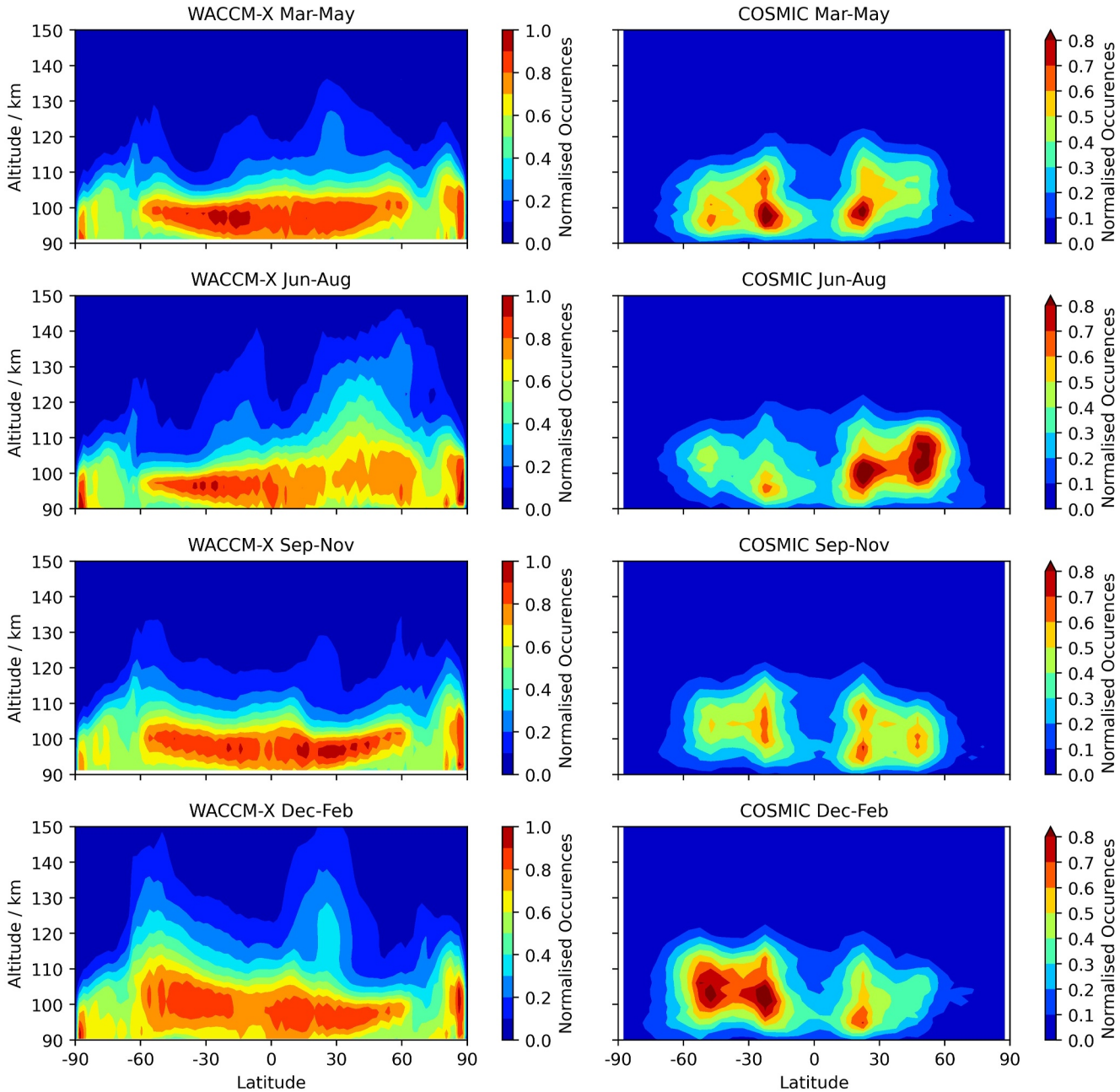

Figure 5. Seasonal altitude-local time distributions of normalized Es layer occurrence, for WACCM-X (left) and COSMIC (right). The seasons are presented from top to bottom, from March-May through to December-February.

Figure 5 displays the altitude-latitude distributions of normalized Es layer occurrence. The normalized occurrence is calculated by adjusting the raw number of Es events identified using the overall maximum and minimum values across all seasons for WACCM and COSMIC datasets separately. This approach is necessary due to the inherent differences in data processing between the COSMIC and WACCM-X methodologies. For COSMIC data, no specific altitude can be assigned to the occultation where an Es layer is not present, since it spans multiple altitudes. As the sampling rates differ between the two datasets, the number of occurrences would show significant disparities. Normalizing ensures the occurrence data are on the same scale, facilitating a more meaningful comparison between COSMIC and WACCM-X. For visualization, WACCM data is displayed on a scale from 0 to 1, while COSMIC data is shown on a scale from 0 to 0.8, with the uppermost color bin representing values

from 0.8 to 1. This allows for a consistent normalization approach while accounting for differences in data ranges and ensuring the clarity of the visualization.

For both COSMIC and WACCM-X, Es occur higher and over a larger vertical extent in the northern hemisphere for June-August (NH summer). Conversely, in December-February (NH winter) the opposite patterns in Es occurrences can be seen, with Es forming at higher altitudes and over a greater vertical extent in the southern (summer) hemisphere. For COSMIC in the summer hemispheres most Es layers are formed in the height range from approximately 90 km to around 115–120 km, whereas in winter this upper limit is reduced to around 110 km. For WACCM-X, though the majority of Es are formed at altitudes of around 90–110 km, the altitude range over which Es form—and particularly the upper altitude limit for Es formation—is more variable, particularly in the summer hemisphere. In both NH and SH summer, the greatest altitude range over which Es are formed is at mid-latitudes, where Es can be found up to altitudes of 130 or even 140 km. At the equinoxes, the altitude-latitude distributions for both COSMIC and WACCM-X are more symmetric about the equator, with more consistent occurrence rates and vertical extent. For COSMIC, the altitude range over which Es layers form is around 5 km higher for the spring hemisphere as compared to the autumn hemisphere in both March-May and September-November. At mid and low-latitudes, this trend is also seen in WACCM-X.

In the COSMIC dataset there is increased Es occurrence for all seasons at mid-latitudes, particularly at around ±20° and ±50°. There is a significant drop in occurrence at high latitudes and around the equator. These areas correlate with the total number of measurements from this technique - a significant increase is seen in the number of occultations at mid-latitudes, with the greatest number of measurements at ±20° and ±50° and significantly fewer at the equator and poles (see Figure S8 in Supporting Information S1). This indicates a possible impact of the measurement methodology on derived distributions. The WACCM-X dataset does not exhibit the same pattern as that seen by COSMIC, instead showing a more consistent occurrence across low and mid latitudes for all seasons, with a decrease in occurrence at around ±70° and an additional population of Es at the poles.

Figure 6 depicts the altitude-local time distributions of Es layer occurrence rates for different latitudinal regions. Rows 1 and 2 represent low latitudes (15–20°) for COSMIC and WACCM-X, respectively, while rows 2 and 4 correspond to mid-latitudes (45–50°). At mid-latitudes, COSMIC-derived occurrence rates exhibit a maximum in Es occurrence in June-August (NH summer) and a minimum in December-February (NH winter). Semidiurnal behavior is exhibited, with Es traces typically descending from around 115–90 km in altitude, beginning at approximately 06:00 and 16:00 local time (LT). Additionally, terdiurnal tides are evident at 90–100 km. In contrast to the mid-latitudes, at low latitudes there is less variation in Es occurrence rates between seasons. Below latitudes of around 30°, and particularly at altitudes below around 100 km, semidiurnal behavior is not clearly discerned, and a diurnal variation is observed with a slower descent rate compared to the semidiurnal tide-induced Es.

At mid-latitudes, the spatio-temporal patterns of the WACCM-X Es traces are similar to those from COSMIC, though the summer maximum in Es occurrence is not as clearly observed as it is in the COSMIC dataset. The influence of the semidiurnal tides is evident, with Es layers descending from approximately 120-130 km down to 90 km, starting around 06:00–09:00 and 16:00 LT. The Es traces in WACCM-X start at slightly higher altitudes compared to the equivalent in the COSMIC data, although the descent rates for both datasets are similar. For all seasons, the daytime trace is typically more intense than the evening trace, which can be attributed to a combination of the increased availability of metallic ions during the day and the influence of both the semidiurnal and diurnal tides (Haldoupis et al., 2007; Pignalberi et al., 2014). Below 30° latitude, the diurnal patterns are also comparable for WACCM-X and COSMIC. However, a faster descent rate is observed in the evening trace for WACCM-X derived Es. Like mid-latitudes, the daytime trace is typically more intense. However, this is not the case for June–August, where the second trace is particularly strong.

The zonal wind shear (dU/dz) mechanism of Es layer formation involves the horizontal magnetic field component and a vertical wind shear characterised by a westward wind above and an eastward wind below. Ions advected by a westward (eastward) wind drift downwards (upwards) in response to the Lorentz force, converging at the wind shear null ($U = 0$) to form a layer (Yamazaki et al., 2022). Figure 7 depicts the altitude-local time distributions of WACCM-X Es occurrence for latitudinal bands 15–20° and 45–50° during NH summer and winter, with U wind fields overlaid as white contour lines, highlighting wind shear zones. At summer mid-latitudes, a strong correlation is observed between Es occurrence and the zero-wind lines ($U = 0$), where the intense wind shear transitions occur from east to west or vice versa. The zero-wind line exhibits semidiurnal behaviour: the morning trace initiates around 06:00 LT, descending from approximately 120–100 km, while the afternoon trace starts at 14:00

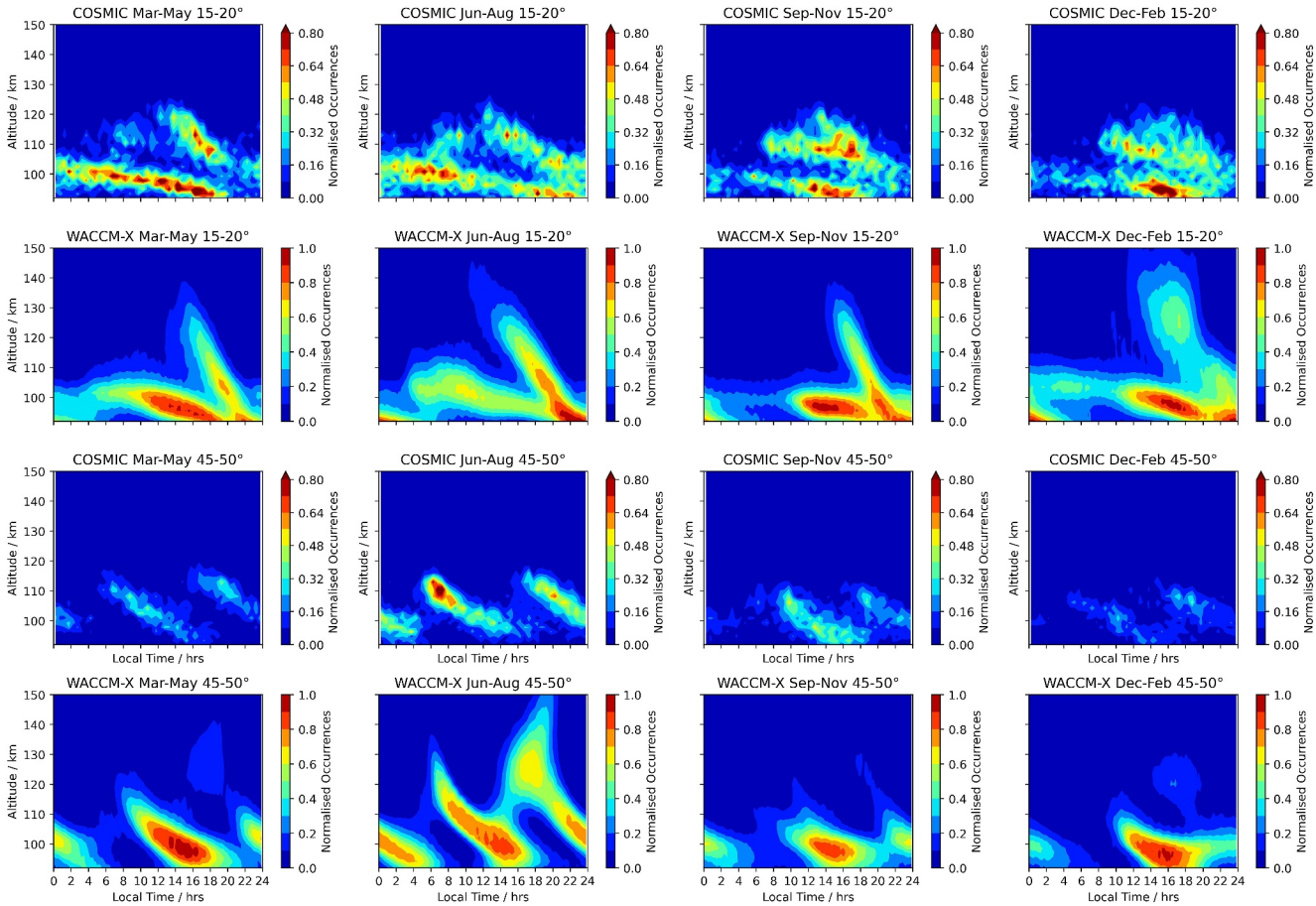

Figure 6. Seasonal altitude-local time distributions of the normalized Es layer occurrence for different latitudinal regions. Rows 1 and 2 show latitudes of 15–20° for COSMIC (top) and WACCM-X (bottom). Rows 3 and 4 show latitudes of 45–50° for COSMIC and WACCM-X (top and bottom respectively). The seasons are presented from left to right, from March-May through to December-February.

LT, descending from about 150 to 100 km. These wind shear zones coincide with identified Es layers, emphasizing the role of semidiurnal tides in modulating Es layer dynamics. In winter and at low latitudes, this correlation is less pronounced but still discernible. Here, the zero-wind line exhibits significant altitude variability; diurnal variations are clearer than semidiurnal ones, with slower descent rates observed below 110 km. Notably, at low latitudes, the faster descent rate in the evening trace for WACCM-X data suggests a nuanced interaction between tides and wind shear.

Figure 8 shows the daily variability of $[M^+]$ and the zonal wind shear at 110 km, dU/dz s^{-1}, for July at a mid- (lat = 47.5°, lon = 180° E, alt = 110 km) and low- (lat = 17.5°, lon = 180°, alt = 110 km) latitude location. At mid-latitudes, there is a strong, regular semidiurnal cycle in the zonal wind. Strong negative wind shears result in a sharp increase in $[M^+]$, highlighting the combined influence of zonal winds and tides. At low latitudes, the zonal winds are more erratic, with no clear repeating pattern in daily variability. Here, the sharp increases in $[M^+]$ are not correlated to the negative shears. This result reflects that the vertical shear of the zonal wind at mid latitudes due to the semidiurnal tide is greater than that at low latitudes due to the diurnal tide, and is in line with previous studies—Es occurrence rates have been shown to correlate with negative vertical shears in the eastward wind (Yamazaki et al., 2022) and neutral wind observations by the Ionospheric Connection Explorer (ICON) satellite demonstrate that strong negative shears in the eastward wind are most frequent in summer midlatitudes (25°N −40°N) (Li et al., 2024). Note that the vertical shear of the meridional wind is also relevant for Es layer formation. However, in the 90–120 km altitude range, where Es layers are typically observed, the vertical ion velocity is primarily driven by the shear of the eastward wind, as studies have shown it has a more dominant influence on ion convergence (Yamazaki et al., 2022).

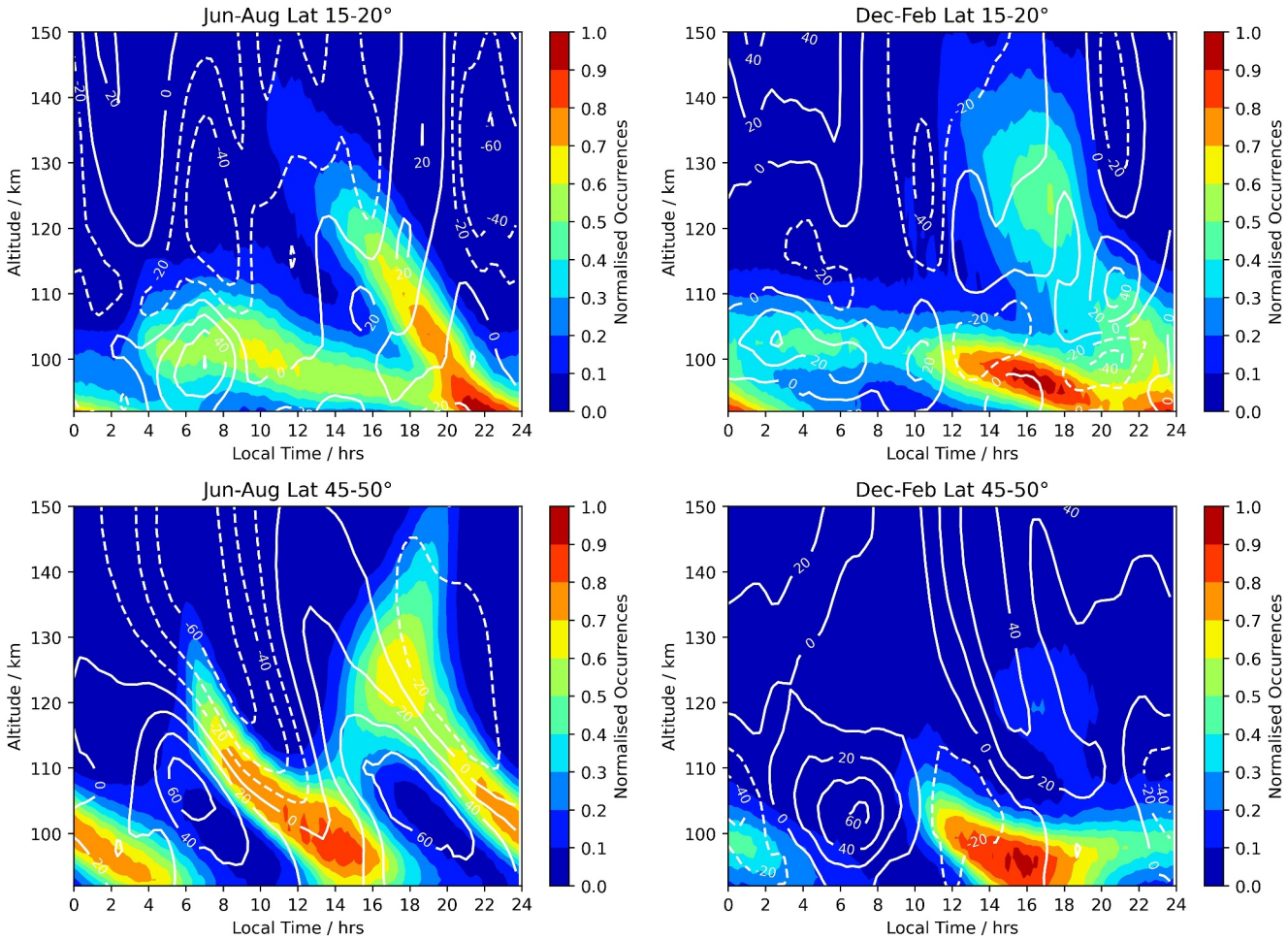

Figure 7. Altitude-local time distributions of the normalized Es layer occurrence (filled contours) and the U winds (white contour lines) for WACCM-X. Rows 1 and 2 show latitudes of 15–20° and 45–50° respectively, columns 1 and 2 show June-August and December-February respectively.

4. Conclusions

This study presents the first study whereby sporadic-E structures are produced self-consistently within a global climate model. A novel algorithm has been developed to identify layers within WACCM-X output based on specified selection criteria. Using this selection process, a comprehensive analysis of Es layer occurrence has been conducted and the climatology presented, with a comparison to Es occurrence rates derived from COSMIC radio-occultation measurements. Through a comparison of Es occurrence rates between the two datasets, several key findings have emerged.

Our analysis highlights the influence of seasonal variability and geomagnetic effects on Es layer formation. Consistent with previous studies, we observe distinct seasonal patterns in Es occurrence, with peaks during summer months and reduced frequencies during winter, reflecting the seasonal modulation of meteoric ion deposition in the upper atmosphere. The alignment of Es occurrence with geomagnetic contours indicates the spatial distribution of the Es layers is substantially geomagnetically controlled.

In line with the COSMIC-derived occurrence rates, WACCM-X produces Es layers mainly during local daytime; for all seasons, a peak in Es occurrence is observed in the afternoon-evening. In the summer hemispheres, Es formation continues throughout local nighttime. In both the northern and southern summer hemispheres, an increase in the peak altitude and vertical extent of Es layers is observed compared to the corresponding winter hemispheres. Differences in the latitudinal distributions are noted between COSMIC and WACCM-X—in COSMIC, the highest occurrence is consistently at mid-latitudes, whereas a significant population of Es layers is also observed at both low and high latitudes for WACCM-X. This discrepancy may be influenced by differing

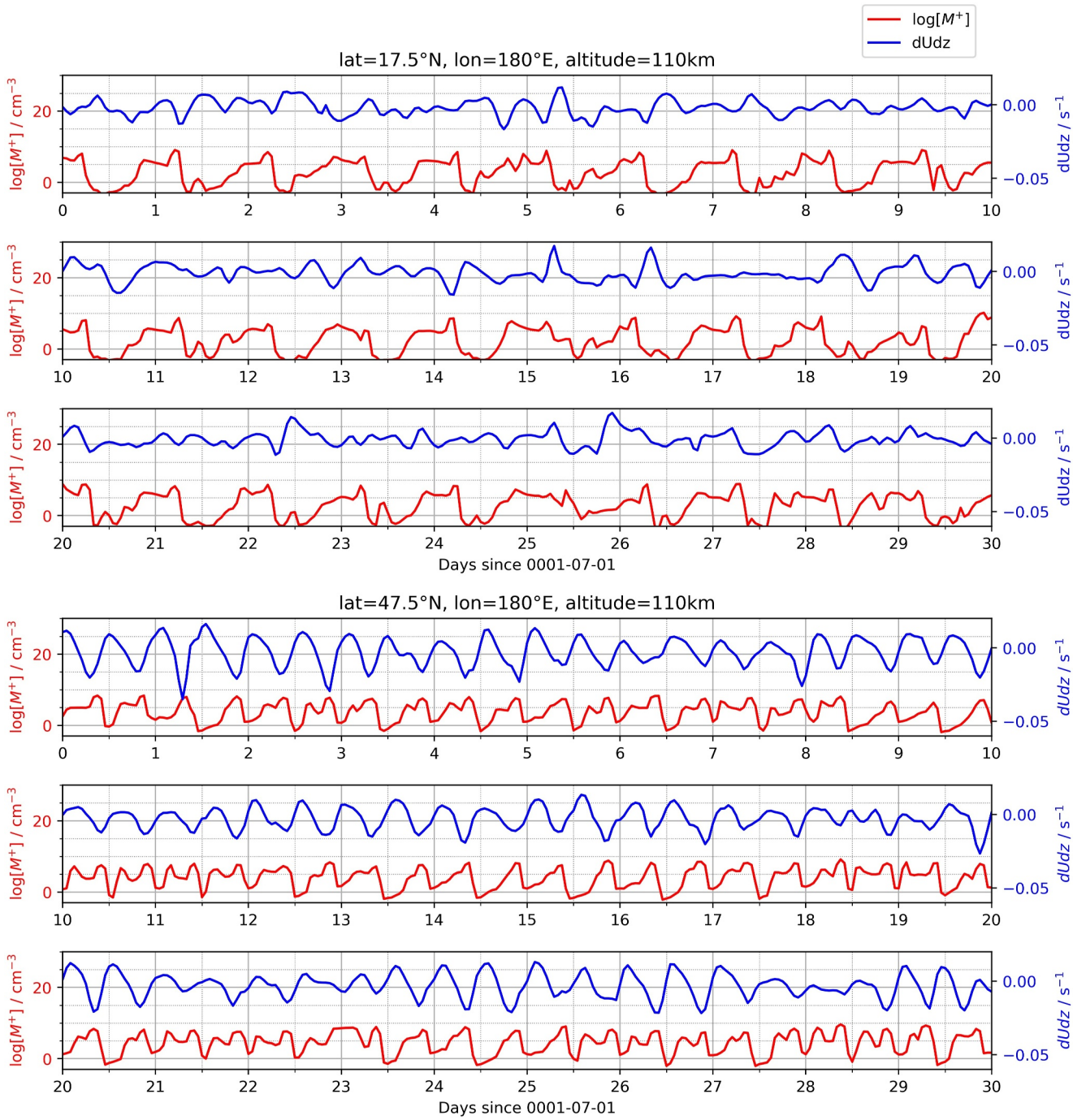

Figure 8. Daily variability of $[M^+]/cm^{-3}$ and the zonal wind shear (dU/dz (s^{-1})) for July at a mid- (lat = 47.5°N, lon = 180°E, alt = 110 km) and low- (lat = 17.5°N, lon = 180°E, alt = 110 km) latitude location.

formation mechanisms of the Es layers, a decreased sensitivity of the WACCM-X identification methodology to low-latitude Es and the availability of high and low latitude measurements from the COSMIC dataset.

The expected diurnal patterns of Es traces are well-captured by WACCM-X, with layers descending with increasing local time. At mid-latitudes, the influence of the semidiurnal tides is dominant, whereas at low latitudes the semidiurnal traces are not clearly defined and the influence of the diurnal tides dominates. Some discrepancies are observed in the descent rate of the second E trace at low latitudes, with a faster descent rate observed for

WACCM-X. The altitude-local time plots reveal significant correlations between Es occurrence and U wind fields at mid-latitudes, highlighting the role of tidal influences and wind shear in modulating Es layer dynamics.

This study enhances the modelling capabilities of sporadic Es and deepens our understanding of their formation. However, we acknowledge the discrepancies that exist with S4-derived Es occurrences, highlighting the ongoing challenges in accurately modelling Sporadic E layers within coupled climate-chemistry models. The differences in the magnitude, timing and location of Es layers between WACCM-X and COSMIC highlight the potential for further enhancement and validation of both the identification algorithm criteria and the parameterisations and processes governing Es layer formation in WACCM-X; further investigation into the complex interplay between atmospheric dynamics, solar activity, climate variability and Es layer formation is warranted to better understand and predict Es layer behaviour.

It may also be possible to use the algorithm for identifying blanketing versus non-blanketing Es layers. However, the model resolution may limit its ability to resolve the finer structures of thin, patchy non-blanketing layers; as a result, grid smoothing could overestimate the thickness of these layers, while localized high-density patches may be averaged out, impacting key parameters such as critical frequency (f_0Es). Implementing a regionally refined version of the model with much higher resolution over specific area of interest, should enable more precise identification of Es characteristics and a better representation of the wind shear and gravity wave dynamics that influence Es formation. This would increase the algorithm's effectiveness in differentiating between blanketing and non-blanketing Es events.

Overall, this study contributes to advancing our understanding of Es layer dynamics and their drivers, providing valuable insights into the formation and variability of these elusive atmospheric phenomena. Through an inter-comparison of atmospheric modelling and satellite data, we have improved our ability to simulate and characterize Es layers. This opens avenues for future research to study their behaviour under different atmospheric conditions and further elucidate the underlying mechanisms driving their formation over different spatio-temporal contexts.

Data Availability Statement

A 1 year WACCM-X simulation was performed on the High Performance Computing (ARC) clusters at the University of Leeds and the output is stored at the PeTAL tape archive.

https://arc.leeds.ac.uk/platforms/.

The COSMIC RO data were downloaded from the FORMOSAT-3/Constellation Observing System for Meteorology Ionosphere and Climate (COSMIC-1) (https://doi.org/10.5065/ZD80-KD74, UCAR COSMIC Program, 2022).

The code base used for the identification algorithm is available on Github at https://github.com/tashaay/SpE_Identification_Notebooks and archived on Zenovo at https://doi.org/10.5281/zenodo.14145588 (Aylett, 2024).

Acknowledgments
This work was supported by the European Office of Aerospace Research and Development (EOARD), award # FA8655-21-1-7031. WF is supported by NCAS National Capability Single Centre Science Programme. DRM and WF are supported by United Kingdom (UK) Natural Environment Research Council (NERC) DRivers and Impacts of Ionospheric Variability with EISCAT-3D (DRIIVE) (NE/W003325/1). DRTs' contributions to this work are supported by US Office of Naval Research PRISM grant N00014-23-S-B001 and the UK NERC DRIIVE (NE/W003317/1) and FINESSE (NE/W003147/1) grants. The authors would like to acknowledge Dr Jianfei Wu (University of Science and Technology of China) for kindly providing WACCM-X data (J Wu et al., 2021) for analysis during initial algorithm development. Likewise, Dr Binkun Yu at USTC has kindly provided their processed COSMIC data for initial use during project development.

References

Abdu, M. A., Batista, I. S., Muralikrishna, P., & Sobral, J. H. A. (1996). Long term trends in sporadic E layers and electric fields over Fortaleza, Brazil. *Geophysical Research Letters*, *23*(7), 757–760. https://doi.org/10.1029/96GL00589

Andoh, S., Saito, A., & Shinagawa, H. (2023). E-field effects on day-to-day variations of geomagnetic mid-latitude sporadic E layers. *Journal of Geophysical Research: Space Physics*, *128*(7), e2022JA031167. https://doi.org/10.1029/2022JA031167

Anthes, R. A., Bernhardt, P. A., Chen, Y., Cucurull, L., Dymond, K. F., Ector, D., et al. (2008). The COSMIC/FORMOSAT-3 mission: Early results. *Bulletin of the American Meteorological Society*, *89*(3), 313–334. https://doi.org/10.1175/BAMS-89-3-313

Arras, C., Jacobi, C., & Wickert, J. (2009). Semidiurnal tidal signature in sporadic E occurrence rates derived from GPS radio occultation measurements at higher midlatitudes. *Annales Geophysicae*, *27*(6), 2555–2563. https://doi.org/10.5194/angeo-27-2555-2009

Arras, C., Resende, L. C. A., Kepkar, A., Senevirathna, G., & Wickert, J. (2022). Sporadic E layer characteristics at equatorial latitudes as observed by GNSS radio occultation measurements. *Earth Planets and Space*, *74*(1), 163. https://doi.org/10.1186/s40623-022-01718-y

Arras, C., & Wickert, J. (2018). Estimation of ionospheric sporadic E intensities from GPS radio occultation measurements. *Journal of Atmospheric and Solar-Terrestrial Physics*, *171*, 60–63. https://doi.org/10.1016/j.jastp.2017.08.006

Arras, C., Wickert, J., Beyerle, G., Heise, S., Schmidt, T., & Jacobi, C. (2008). A global climatology of ionospheric irregularities derived from GPS radio occultation. *Geophysical Research Letters*, *35*(14), L14809. https://doi.org/10.1029/2008GL034158

Axford, W. I. (1963). Formation and vertical movement of dense ionized layers in ionosphere due to neutral wind shears. *Journal of Geophysical Research*, *68*(3), 769–779. https://doi.org/10.1029/JZ068i003p00769

Aylett. (2024). SpE_Identification_Notebooks_v1 [Software]. *Zenodo*. https://doi.org/10.5281/zenodo.14145588

Bones, D. L., Plane, J. M., & Feng, W. (2016). Dissociative recombination of FeO(+) with electrons: Implications for plasma layers in the ionosphere. *Journal of Physical Chemistry A*, *120*(9), 1369–1376. https://doi.org/10.1021/acs.jpca.5b04947

Cameron, T. G., Fiori, R. A. D., Themens, D. R., Warrington, E. M., Thayaparan, T., & Galeschuk, D. (2022). Evaluation of the effect of sporadic-E on high frequency radio wave propagation in the Arctic. *Journal of Atmospheric and Solar-Terrestrial Physics*, *228*, 105826. https://doi.org/10.1016/j.jastp.2022.105826

Carmona, R. A., Nava, O. A., Dao, E. V., & Emmons, D. J. (2022). A comparison of sporadic-e occurrence rates using gps radio occultation and ionosonde measurements. *Remote Sensing*, *14*(3), 581. https://doi.org/10.3390/rs14030581

Carrillo-Sánchez, J. D., Gómez-Martín, J. C., Bones, D. L., Nesvorný, D., Pokorný, P., Benna, M., et al. (2020). Cosmic dust fluxes in the atmospheres of Earth, Mars, and Venus. *Icarus*, *335*, 113395. https://doi.org/10.1016/j.icarus.2019.113395

Chartier, A. T., Hanley, T. R., & Emmons, D. J. (2022). Long-distance propagation of 162 MHz shipping information links associated with sporadic E. *Atmospheric Measurement Techniques*, *15*(21), 6387–6393. https://doi.org/10.5194/amt-15-6387-2022

Chu, Y. H., Wang, C. Y., Wu, K. H., Chen, K. T., Tzeng, K. J., Su, C. L., et al. (2014). Morphology of sporadic E layer retrieved from COSMIC GPS radio occultation measurements: Wind shear theory examination. *Journal of Geophysical Research: Space Physics*, *119*(3), 2117–2136. https://doi.org/10.1002/2013ja019437

Cox, R. M., & Plane, J. M. C. (1998). An ion-molecule mechanism for the formation of neutral sporadic Na layers. *Journal of Geophysical Research*, *103*(D6), 6349–6359. https://doi.org/10.1029/97JD03376

Cullens, C. Y., England, S. L., & Garcia, R. R. (2016). The 11 year solar cycle signature on wave-driven dynamics in WACCM. *Journal of Geophysical Research: Space Physics*, *121*(4), 3484–3496. https://doi.org/10.1002/2016JA022455

Dieterich, J. C., Nott, G. J., Espy, P. J., Chu, X., & Riggin, D. (2006). Statistics of sporadic iron layers and relation to atmospheric dynamics. *Journal of Atmospheric and Solar-Terrestrial Physics*, *68*(1), 102–113. https://doi.org/10.1016/j.jastp.2005.08.008

Djuth, F. T., Zhang, L. D., Livneh, D. J., Seker, I., Smith, S. M., Sulzer, M. P., et al. (2010). Arecibo's thermospheric gravity waves and the case for an ocean source. *Journal of Geophysical Research*, *115*(A8), A08305. https://doi.org/10.1029/2009JA014799

Ellis, J. A., Emmons, D. J., & Cohen, M. B. (2024). Detection and classification of sporadic E using convolutional Neural Networks. *Space Weather*, *22*(1), e2023SW003669. https://doi.org/10.1029/2023SW003669

Emmons, D. J., Wu, D. L., Swarnalingam, N., Ali, A. F., Ellis, J. A., Fitch, K. E., & Obenberger, K. S. (2023). Improved models for estimating sporadic-E intensity from GNSS radio occultation measurements. *Frontiers in Astronomy and Space Sciences*, *10*, 1327979. https://doi.org/10.3389/fspas.2023.1327979

Fan, Z. Y., Plane, J. M. C., & Gumbel, J. (2007). On the global distribution of sporadic sodium layers. *Geophysical Research Letters*, *34*(15), L15808. https://doi.org/10.1029/2007GL030542

Farley, D. T. (1985). Theory of equatorial electrojet plasma-waves - new developments and current status. *Journal of Atmospheric and Terrestrial Physics*, *47*(8–10), 729–744. https://doi.org/10.1016/0021-9169(85)90050-9

Feng, W., Höffner, J., Marsh, D. R., Chipperfield, M. P., Dawkins, E. C. M., Viehl, T. P., & Plane, J. M. C. (2015). Diurnal variation of the potassium layer in the upper atmosphere. *Geophysical Research Letters*, *42*(9), 3619–3626. https://doi.org/10.1002/2015GL063718

Feng, W., Marsh, D. R., Chipperfield, M. P., Janches, D., Höffner, J., Yi, F., & Plane, J. M. C. (2013). A global atmospheric model of meteoric iron. *Journal of Geophysical Research: Atmospheres*, *118*(16), 9456–9474. https://doi.org/10.1002/jgrd.50708

Fernandez-Prades, C., Presti, L. L., & Falletti, E. (2011). Satellite radiolocalization from GPS to GNSS and beyond: Novel technologies and applications for civil mass market. *Proceedings of the IEEE*, *99*(11), 1882–1904. https://doi.org/10.1109/JPROC.2011.2158032

Fontes, P. A., Muella, M. T. A. H., Resende, L. C. A., & Fagundes, P. R. (2024). Evidence of anti-correlation between sporadic (Es) layers occurrence and solar activity observed at low latitudes over the Brazilian sector. *Advances in Space Research*, *73*(7), 3563–3577. https://doi.org/10.1016/j.asr.2023.09.040

Garcia, R. R., Smith, A. K., Kinnison, D. E., Cámara, Á. d. l., & Murphy, D. J. (2017). Modification of the gravity wave parameterization in the whole atmosphere community climate model: Motivation and results. *Journal of the Atmospheric Sciences*, *74*(1), 275–291. https://doi.org/10.1175/JAS-D-16-0104.1

Gooch, J. Y., Colman, J. J., Nava, O. A., & Emmons, D. J. (2020). Global ionosonde and GPS radio occultation sporadic-E intensity and height comparison. *Journal of Atmospheric and Solar-Terrestrial Physics*, *199*, 105200. https://doi.org/10.1016/j.jastp.2020.105200

Haldoupis, C. (2012). Midlatitude sporadic E. A typical paradigm of atmosphere-ionosphere coupling. *Space Science Reviews*, *168*(1), 441–461. https://doi.org/10.1007/s11214-011-9786-8

Haldoupis, C. (2019). An improved ionosonde-based parameter to assess sporadic E layer intensities: A simple idea and an algorithm. *Journal of Geophysical Research: Space Physics*, *124*(3), 2127–2134. https://doi.org/10.1029/2018JA026441

Haldoupis, C., Meek, C., Christakis, N., Pancheva, D., & Bourdillon, A. (2006). Ionogram height-time-intensity observations of descending sporadic E layers at mid-latitude. *Journal of Atmospheric and Solar-Terrestrial Physics*, *68*(3–5), 539–557. https://doi.org/10.1016/j.jastp.2005.03.020

Haldoupis, C., Pancheva, D., Singer, W., Meek, C., & MacDougall, J. (2007). An explanation for the seasonal dependence of midlatitude sporadic E layers. *Journal of Geophysical Research*, *112*(A6), A06315. https://doi.org/10.1029/2007JA012322

Hocke, K., & Tsuda, T. (2001). Gravity waves and ionospheric irregularities over tropical convection zones observed by GPS/MET Radio Occultation. *Geophysical Research Letters*, *28*(14), 2815–2818. https://doi.org/10.1029/2001GL013076

Hodos, T. J., Nava, O. A., Dao, E. V., & Emmons, D. J. (2022). Global sporadic-E occurrence rate climatology using GPS radio occultation and ionosonde data. *Journal of Geophysical Research: Space Physics*, *127*(12), e2022JA030795. https://doi.org/10.1029/2022JA030795

Hu, T. Y., Luo, J., & Xu, X. H. (2022). Deriving ionospheric sporadic E intensity from FORMOSAT-3/COSMIC and FY-3C radio occultation measurements. *Space Weather-the International Journal of Research and Applications*, *20*(12), e2022SW003214. https://doi.org/10.1029/2022sw003214

Huba, J. D., Krall, J., & Drob, D. (2019). Global ionospheric metal ion transport with Sami3. *Geophysical Research Letters*, *46*(14), 7937–7944. https://doi.org/10.1029/2019GL083583

Hurrell, J. W., Holland, M. M., Gent, P. R., Ghan, S., Kay, J. E., Kushner, P. J., et al. (2013). The community Earth system model: A framework for collaborative research. *Bulletin of the American Meteorological Society*, *94*(9), 1339–1360. https://doi.org/10.1175/BAMS-D-12-00121.1

Hysell, D. L., Yamamoto, M., & Fukao, S. (2002). Simulations of plasma clouds in the midlatitude E region ionosphere with implications for type I and type II quasiperiodic echoes. *Journal of Geophysical Research*, *107*(A10), SIA 17-1–SIA 17-9. https://doi.org/10.1029/2002ja009291

Janches, D., Heinselman, C. J., Chau, J. L., Chandran, A., & Woodman, R. (2006). Modeling the global micrometeor input function in the upper atmosphere observed by high power and large aperture radars. *Journal of Geophysical Research*, *111*(A7), A07317. https://doi.org/10.1029/2006JA011628

Kintner, P. M., Ledvina, B. M., & De Paula, E. R. (2007). GPS and ionospheric scintillations. *Space Weather*, *5*(9), S09003. https://doi.org/10.1029/2006SW000260

Kirkwood, S., & Nilsson, H. (2000). High-latitude sporadic-E and other thin layers – The role of magnetospheric electric fields. *Space Science Reviews*, *91*(3), 579–613. https://doi.org/10.1023/A:1005241931650

Kotadia, K. M. (1969). Sporadic-E ionization over Ahmedabad through the half solar cycle 1954–1957. *Journal of Atmospheric and Terrestrial Physics*, *31*(9), 1137–1146. https://doi.org/10.1016/0021-9169(69)90050-6

Krall, J., Huba, J. D., Nossa, E., Aponte, N., & Drob, D. P. (2020). Sami3 simulations of ionospheric metallic layers at Arecibo. *Journal of Geophysical Research: Space Physics*, *125*(3), e2019JA027297. https://doi.org/10.1029/2019JA027297

Langowski, M. P., Von Savigny, C., Burrows, J. P., Feng, W., Plane, J. M. C., Marsh, D. R., et al. (2015). Global investigation of the Mg atom and ion layers using SCIAMACHY/Envisat observations between 70 and 150 km altitude and WACCM-Mg model results. *Atmospheric Chemistry and Physics*, *15*(1), 273–295. https://doi.org/10.5194/acp-15-273-2015

Layzer, D. (1972). Theory of midlatitude sporadic E. *Radio Science*, *7*(3), 385–395. https://doi.org/10.1029/RS007i003p00385

Li, M., Deng, Y., Harding, B. J., & England, S. (2024). Climatology of dayside E-region zonal neutral wind shears from ICON-mighti observations. *Space Weather*, *22*(2), e2023SW003670. https://doi.org/10.1029/2023SW003670

Liu, H.-L., Bardeen, C. G., Foster, B. T., Lauritzen, P., Liu, J., Lu, G., et al. (2018). Development and validation of the whole atmosphere community climate model with thermosphere and ionosphere extension. *WACCM-X 2.0*, *10*(2), 381–402. https://doi.org/10.1002/2017MS001232

Liu, J., Liu, H., Wang, W., Burns, A. G., Wu, Q., Gan, Q., et al. (2018). First results from the ionospheric extension of WACCM-X during the deep solar minimum Year of 2008. *J Geophys ResSpace*, *123*(2), 1534–1553. https://doi.org/10.1002/2017ja025010

MacDougall, J. W., & Jayachandran, P. T. (2005). Sporadic E at cusp latitudes. *Journal of Atmospheric and Solar-terrestrial Physics*, *67*(15), 1419–1426. https://doi.org/10.1016/j.jastp.2005.07.011

MacDougall, J. W., Jayachandran, P. T., & Plane, J. M. C. (2000). Polar cap sporadic-E: Part 1, observations. *Journal of Atmospheric and Solar-Terrestrial Physics*, *62*(13), 1155–1167. https://doi.org/10.1016/S1364-6826(00)00093-6

Marsh, D. R., Janches, D., Feng, W., & Plane, J. M. C. (2013). A global model of meteoric sodium. *Journal of Geophysical Research: Atmospheres*, *118*(19), 11442–11452. https://doi.org/10.1002/jgrd.50870

Marsh, D. R., Mills, M. J., Kinnison, D. E., Lamarque, J.-F., Calvo, N., & Polvani, L. M. (2013). Climate change from 1850 to 2005 simulated in CESM1 (WACCM). *Journal of Climate*, *26*(19), 7372–7391. https://doi.org/10.1175/JCLI-D-12-00558.1

Mathews, J. D. (1998). Sporadic E: Current views and recent progress. *Journal of Atmospheric and Solar-Terrestrial Physics*, *60*(4), 413–435. https://doi.org/10.1016/s1364-6826(97)00043-6

Matzka, J., Stolle, C., Yamazaki, Y., Bronkalla, O., & Morschhauser, A. (2021). The geomagnetic Kp index and derived indices of geomagnetic activity. *Space Weather*, *19*(5), e2020SW002641. https://doi.org/10.1029/2020SW002641

Neale, R. B., Richter, J., Park, S., Lauritzen, P. H., Vavrus, S. J., Rasch, P. J., & Zhang, M. (2013). The mean climate of the community atmosphere model (CAM4) in forced SST and fully coupled experiments. *Journal of Climate*, *26*(14), 5150–5168. https://doi.org/10.1175/JCLI-D-12-00236.1

Niu, J., Weng, L. B., Meng, X., & Fang, H. X. (2019). Morphology of ionospheric sporadic E layer intensity based on COSMIC occultation data in the midlatitude and low-latitude regions. *Journal of Geophysical Research: Space Physics*, *124*(6), 4796–4808. https://doi.org/10.1029/2019JA026828

Nygrén, T., Jalonen, L., Oksman, J., & Turunen, T. (1984). The role of electric field and neutral wind direction in the formation of sporadic E-layers. *Journal of Atmospheric and Terrestrial Physics*, *46*(4), 373–381. https://doi.org/10.1016/0021-9169(84)90122-3

Oikonomou, C., Haralambous, H., Haldoupis, C., & Meek, C. (2014). Sporadic E tidal variabilities and characteristics observed with the Cyprus Digisonde. *Journal of Atmospheric and Solar-Terrestrial Physics*, *119*, 173–183. https://doi.org/10.1016/j.jastp.2014.07.014

Oyinloye, J. O. (1969). A comparison study of the occurrence of equatorial type Es and daytime blanketing Es in the magnetic equatorial zone. *Radio Science*, *4*(9), 765–769. https://doi.org/10.1029/RS004i009p00765

Pavelyev, A. G., Liou, Y. A., Wickert, J., Schmidt, T., Pavelyev, A. A., & Liu, S. F. (2007). Effects of the ionosphere and solar activity on radio occultation signals: Application to CHAllenging Minisatellite Payload satellite observations. *Journal of Geophysical Research*, *112*(A6), A06326. https://doi.org/10.1029/2006JA011625

Pedatella, N. M. (2016). Impact of the lower atmosphere on the ionosphere response to a geomagnetic superstorm. *Geophysical Research Letters*, *43*(18), 9383–9389. https://doi.org/10.1002/2016GL070592

Pedatella, N. M., Chau, J. L., Vierinen, J., Qian, L., Reyes, P., Kudeki, E., et al. (2019). Solar flare effects on 150-km echoes observed over Jicamarca: WACCM-X simulations. *Geophysical Research Letters*, *46*(20), 10951–10958. https://doi.org/10.1029/2019GL084790

Pezzopane, M., Pignalberi, A., & Pietrella, M. (2015). On the influence of solar activity on the mid-latitude sporadic E layer. *Journal of Space Weather and Space Climate*, *5*, A31. https://doi.org/10.1051/swsc/2015031

Pignalberi, A., Pezzopane, M., & Zuccheretti, E. (2014). Sporadic E layer at mid-latitudes: Average properties and influence of atmospheric tides. *Annals of Geophysics*, *32*(11), 1427–1440. https://doi.org/10.5194/angeo-32-1427-2014

Plane, J. M. C. (2003). Atmospheric chemistry of meteoric metals. *Chemical Reviews*, *103*(12), 4963–4984. https://doi.org/10.1021/cr0205309

Plane, J. M. C., Feng, W., & Dawkins, E. C. M. (2015). The mesosphere and metals: Chemistry and changes. *Chemical Reviews*, *115*(10), 4497–4541. https://doi.org/10.1021/cr500501m

Qiu, L., Yamazaki, Y., Yu, T., Becker, E., Miyoshi, Y., Qi, Y., et al. (2023). Numerical simulations of metallic ion density perturbations in sporadic E layers caused by gravity waves. *Earth and Space Science*, *10*(8), e2023EA003030. https://doi.org/10.1029/2023EA003030

Raghavarao, R., Patra, A. K., & Sripathi, S. (2002). Equatorial E region irregularities: A review of recent observations. *Journal of Atmospheric and Solar-Terrestrial Physics*, *64*(12), 1435–1443. https://doi.org/10.1016/S1364-6826(02)00107-4

Rao, C. S. R. (1964). Sporadic-E and the equatorial electrojet. *Journal of Atmospheric and Terrestrial Physics*, *26*(3), 417–427. https://doi.org/10.1016/0021-9169(64)90088-1

Resende, L. C. A., Batista, I. S., Denardini, C. M., Batista, P. P., Carrasco, A. J., Andrioli, V. d. F., & Moro, J. (2017). Simulations of blanketing sporadic E-layer over the Brazilian sector driven by tidal winds. *Journal of Atmospheric and Solar-Terrestrial Physics*, *154*, 104–114. https://doi.org/10.1016/j.jastp.2016.12.012

Richter, J. H., Sassi, F., & Garcia, R. R. (2010). Toward a physically based gravity wave source Parameterization in a general circulation model. *Journal of the Atmospheric Sciences*, *67*(1), 136–156. https://doi.org/10.1175/2009JAS3112.1

Shinagawa, H., Miyoshi, Y., Jin, H., & Fujiwara, H. (2017). Global distribution of neutral wind shear associated with sporadic E layers derived from GAIA. *Journal of Geophysical Research: Space Physics*, *122*(4), 4450–4465. https://doi.org/10.1002/2016JA023778

Shinagawa, H., Tao, C., Jin, H., Miyoshi, Y., & Fujiwara, H. (2021). Numerical prediction of sporadic E layer occurrence using GAIA. *Earth Planets and Space*, *73*(1), 28. https://doi.org/10.1186/s40623-020-01330-y

Sivakandan, M., Mielich, J., Renkwitz, T., Chau, J. L., Jaen, J., & Laštovička, J. (2023). Long-term variations and residual trends in the E, F, and sporadic E (Es) layer over Juliusruh, Europe. *Journal of Geophysical Research: Space Physics*, *128*(4), e2022JA031097. https://doi.org/10.1029/2022JA031097

Sobhkhiz-Miandehi, S., Yamazaki, Y., Arras, C., & Themens, D. (2023). A comparison of FORMOSAT-3/COSMIC radio occultation and ionosonde measurements in sporadic E detection over mid- and low-latitude regions. *Frontiers in Astronomy and Space Sciences*, *10*, 1198071. https://doi.org/10.3389/fspas.2023.1198071

Solomon, S. C., Liu, H.-L., Marsh, D. R., McInerney, J. M., Qian, L., & Vitt, F. M. (2019). Whole atmosphere climate change: Dependence on solar activity. *Journal of Geophysical Research: Space Physics*, *124*(5), 3799–3809. https://doi.org/10.1029/2019JA026678

Tapping, K. F. (2013). The 10.7 cm solar radio flux (F10.7). *Space Weather*, *11*(7), 394–406. https://doi.org/10.1002/swe.20064

Thayer, J. P., & Semeter, J. (2004). The convergence of magnetospheric energy flux in the polar atmosphere. *Journal of Atmospheric and Solar-Terrestrial Physics*, *66*(10), 807–824. https://doi.org/10.1016/j.jastp.2004.01.035

Tian, P., Yu, B., Ye, H., Xue, X., Wu, J., & Chen, T. (2023). Ionospheric irregularity reconstruction using multisource data fusion via deep learning. *Atmospheric Chemistry and Physics*, *23*(20), 13413–13431. https://doi.org/10.5194/acp-23-13413-2023

Tsunoda, R. T. (2008). On blanketing sporadic E and polarization effects near the equatorial electrojet. *Journal of Geophysical Research*, *113*(A9), A09304. https://doi.org/10.1029/2008JA013158

UCAR COSMIC Program. (2022). COSMIC-1 data products [dataset]. *UCAR/NCAR - COSMIC*. https://doi.org/10.5065/ZD80-KD74

Vial, F. (1993). *Causes of tidal variability, in coupling processes in the lower and middle atmosphere, edited by E. V. Thrane, T. A. Blix and D. C. Fritts* (pp. 137–151). Springer Netherlands. https://doi.org/10.1007/978-94-011-1594-0_9

Viehl, T. P., Plane, J. M. C., Feng, W., & Höffner, J. (2016). The photolysis of FeOH and its effect on the bottomside of the mesospheric Fe layer. *Geophysical Research Letters*, *43*(3), 1373–1381. https://doi.org/10.1002/2015GL067241

Wang, Y., Jayachandran, P. T., Themens, D. R., McCaffrey, A. M., Zhang, Q.-H., David, S., & Chadwick, R. (2021). A case study of polar cap sporadic-E layer associated with TEC variations. *Remote Sensing*, *13*(7), 1324. https://doi.org/10.3390/rs13071324

Wang, Y., Themens, D. R., Wang, C., Ma, Y.-Z., Reimer, A., Varney, R., et al. (2022). Simultaneous observations of a polar cap sporadic-E layer by twin incoherent scatter radars at resolute. *Journal of Geophysical Research: Space Physics*, *127*(6), e2022JA030366. https://doi.org/10.1029/2022JA030366

Whitehead, J. (1961). formation of sporadic-e layer in temperate zones. *Journal of Atmospheric and Terrestrial Physics*, *20*(1), 49–58. https://doi.org/10.1016/0021-9169(61)90097-6

Whitehead, J. D. (1989). Recent work on mid-latitude and equatorial sporadic-E. *Journal of Atmospheric and Terrestrial Physics*, *51*(5), 401–424. https://doi.org/10.1016/0021-9169(89)90122-0

Wu, D. L., Ao, C. O., Hajj, G. A., De La Torre Juarez, M., & Mannucci, A. J. (2005). Sporadic E morphology from GPS-CHAMP radio occultation. *Journal of Geophysical Research*, *110*(A1), A01306. https://doi.org/10.1029/2004JA010701

Wu, J., Feng, W., Liu, H., Xue, X., Marsh, D. R., & Plane, J. M. C. (2021). Self-consistent global transport of metallic ions with WACCM-X. *Atmospheric Chemistry and Physics*, *21*(20), 15619–15630. https://doi.org/10.5194/acp-21-15619-2021

Yamazaki, Y., Arras, C., Andoh, S., Miyoshi, Y., Shinagawa, H., Harding, B. J., et al. (2022). Examining the wind shear theory of sporadic E with ICON/MIGHTI winds and COSMIC-2 radio occultation data. *Geophysical Research Letters*, *49*(1), e2021GL096202. https://doi.org/10.1029/2021GL096202

Ye, H., Xue, X., Yu, T., Sun, Y.-Y., Yi, W., Long, C., et al. (2021). Ionospheric F-layer scintillation variabilities over the American sector during sudden stratospheric warming events. *Space Weather*, *19*(8), e2020SW002703. https://doi.org/10.1029/2020SW002703

Yu, B., Scott, C. J., Xue, X., Yue, X., & Dou, X. (2020). Using GNSS radio occultation data to derive critical frequencies of the ionospheric sporadic E layer in real time. *GPS Solutions*, *25*(1), 14. https://doi.org/10.1007/s10291-020-01050-6

Yu, B., Scott, C. J., Xue, X., Yue, X., & Dou, X. (2021). Derivation of global ionospheric Sporadic E critical frequency (foEs) data from the amplitude variations in GPS/GNSS radio occultations. *Royal Society Open Science*, *7*(7), 200320. https://doi.org/10.1098/rsos.200320

Yu, B., Xue, X., Scott, C. J., Wu, J., Yue, X., Feng, W., et al. (2021). Interhemispheric transport of metallic ions within ionospheric sporadic E layers by the lower thermospheric meridional circulation. *Atmospheric Chemistry and Physics*, *21*(5), 4219–4230. https://doi.org/10.5194/acp-21-4219-2021

Yu, B., Xue, X., Scott, C. J., Yue, X., & Dou, X. (2022). An empirical model of the ionospheric sporadic E layer based on GNSS radio occultation data. *Space Weather*, *20*(8), e2022SW003113. https://doi.org/10.1029/2022SW003113

Yu, B., Xue, X., Yue, X., Yang, C., Yu, C., Dou, X., et al. (2019). The global climatology of the intensity of the ionospheric sporadic E layer. *Atmospheric Chemistry and Physics*, *19*(6), 4139–4151. https://doi.org/10.5194/acp-19-4139-2019

Yue, X. A., Schreiner, W. S., Pedatella, N. M., & Kuo, Y. H. (2016). Characterizing GPS radio occultation loss of lock due to ionospheric weather. *Space Weather-the International Journal of Research and Applications*, *14*(4), 285–299. https://doi.org/10.1002/2015sw001340

Zeng, Z., & Sokolovskiy, S. (2010). Effect of sporadic E clouds on GPS radio occultation signals. *Geophysical Research Letters*, *37*(18), L18817. https://doi.org/10.1029/2010GL044561

Zhang, Y., Wu, J., Guo, L., Hu, Y., Zhao, H., & Xu, T. (2015). Influence of solar and geomagnetic activity on sporadic-E layer over low, mid and high latitude stations. *Advances in Space Research*, *55*(5), 1366–1371. https://doi.org/10.1016/j.asr.2014.12.010

Zhou, X., Li, Z. Z., Yue, X. A., Liu, L. B., & Liu, L. (2024). Effects of mesoscale gravity waves on sporadic E simulated by a one dimensional dynamic model. *Earth Planetary Physics*, *8*(4), 1–9. https://doi.org/10.26464/epp2024038

Zuo, X.-M., & Wan, W.-X. (2002). The correlation between sporadic E-layers and solar Activities. *Chinese Journal of Geophysics*, *45*(6), 803–809. https://doi.org/10.1002/cjg2.295